The Unknown Hydrogen Exosphere: Space Weather Implications

Article *in* Space Weather · February 2018

DOI: 10.1002/2017SW001780

CITATIONS
31

READS
299

5 authors, including:

Jonathan Krall

200 PUBLICATIONS **7,935** CITATIONS

SEE PROFILE

Mei-Ching Fok

298 PUBLICATIONS **5,302** CITATIONS

SEE PROFILE

Joseph D Huba

Syntek Technologies Inc

433 PUBLICATIONS **12,075** CITATIONS

SEE PROFILE

AGU PUBLICATIONS

Space Weather

RESEARCH ARTICLE
10.1002/2017SW001780

The Unknown Hydrogen Exosphere: Space Weather Implications

J. Krall[1], A. Glocer[2], M.-C. Fok[2], S. M. Nossal[3], and J. D. Huba[1]

[1]Plasma Physics Division, Naval Research Laboratory, Washington, DC, USA, [2]NASA Goddard Space Flight Center, Greenbelt, MD, USA, [3]Department of Physics, University of Wisconsin-Madison, Madison, WI, USA

Key Points:
- The hydrogen density in the exosphere and geocorona can deviate significantly from commonly used models; improved models are needed
- The plasmasphere is sensitive to exosphere composition; modeling shows that more hydrogen in the exosphere leads to faster poststorm recovery
- The ring current is sensitive to hydrogen in the magnetosphere; modeling shows that more hydrogen leads to briefer storms

Supporting Information:
- Supporting Information S1
- Data Set S1
- Data Set S2
- Data Set S3
- Data Set S4
- Data Set S5
- Data Set S6
- Data Set S7
- Data Set S8
- Data Set S9
- Data Set S10

Correspondence to:
J. Krall,
jonathan.krall@nrl.navy.mil

Citation:
Krall, J., Glocer, A., Fok, M.-C., Nossal, S. M., & Huba, J. D. (2018). The unknown hydrogen exosphere: Space weather implications. *Space Weather*, *16*, 205–215. https://doi.org/10.1002/2017SW001780

Received 21 NOV 2017
Accepted 30 JAN 2018
Accepted article online 6 FEB 2018
Published online 2 MAR 2018

Abstract Recent studies suggest that the hydrogen (H) density in the exosphere and geocorona might differ from previously assumed values by factors as large as 2. We use the SAMI3 (Sami3 is Also a Model of the Ionosphere) and Comprehensive Inner Magnetosphere-Ionosphere models to evaluate scenarios where the hydrogen density is reduced or enhanced, by a factor of 2, relative to values given by commonly used empirical models. We show that the rate of plasmasphere refilling following a geomagnetic storm varies nearly linearly with the hydrogen density. We also show that the ring current associated with a geomagnetic storm decays more rapidly when H is increased. With respect to these two space weather effects, increased exosphere hydrogen density is associated with reduced threats to space assets during and following a geomagnetic storm.

Plain Language Summary Commonly used empirical models of the hydrogen density in the outer reaches of Earth's atmosphere, the exosphere, may be off by factors as large as two. We use the SAMI3 (Sami3 is Also a Model of the Ionosphere) and CIMI (Comprehensive Inner Magnetosphere-Ionosphere) models to evaluate situations where the model hydrogen density is reduced or enhanced, by a factor of 2, relative to these empirical models. We show that the rate at which the inner magnetosphere plasma density recovers following a geomagnetic storm varies nearly linearly with the hydrogen density. We also show that the ring current associated with a geomagnetic storm decays more rapidly when there is more hydrogen. Overall, increased exosphere hydrogen density is associated with reduced threats to space assets during and following a geomagnetic storm.

1. Introduction

Basic physical processes that contribute to space weather are sensitive to the composition of the outermost layer of Earth's atmosphere, known as the exosphere, and the extension of the hydrogen exosphere into the inner magnetosphere, often called the geocorona. For example, Ilie et al. (2013) calculated that the ring current, a current system in the inner magnetosphere induced during a geomagnetic storm, decays more rapidly if the hydrogen (H) density increases. The ring current is a measure of the strength of a geomagnetic storm and is part of a current system that flows through the middle to high-latitude ionosphere. These ionospheric currents can damage power systems on Earth (Schrijver et al., 2014). Another study (Krall & Huba, 2016) showed the impact of exosphere composition on the plasmasphere. The plasmasphere is the extension of ionosphere plasma into the inner magnetosphere, held in place by closed geomagnetic field lines (Carpenter, 1966). That study showed that the oxygen (O) density in the thermosphere and exosphere affects the flow of plasma into the plasmasphere following a geomagnetic storm, known as the refilling rate (Banks et al., 1971). This is important because increased plasmaspheric density tends to increase the rate at which the radiation belts decay, reducing their space weather impacts (Bortnik & Thorne, 2007; Millan & Thorne, 2007).

The present work is a sensitivity study using first-principle numerical simulation codes. We evaluate the importance of the background H density to the dynamics of the plasmasphere and ring current. It is our hope that this work will be of interest to scientists and program managers that are doing the important work of developing the next generation of space weather prediction models.

1.1. Plasmasphere Contributions to Space Weather

The plasmasphere density has two possibly significant effects on space weather. During a storm the plasmasphere can form a plume that extends sunward toward the magnetopause. If the plume increases the local

plasma density in the region where solar wind magnetic field is reconnecting with Earth's magnetic field, it can reduce the rate of reconnection (Borovsky et al., 2013). This could reduce the severity of the storm, though this effect has yet to be directly observed.

During a storm, the plasmasphere erodes, with the plasmapause moving inward, typically to $L = 2–3$ in tens of minutes (Goldstein et al., 2003). As the plasmasphere density recovers following the storm, the increasing density has the effect of causing the radiation belts to decay. The plasmasphere supports plasma waves that scatter ring current and radiation belt particles (Bortnik & Thorne, 2007; Millan & Thorne, 2007), effectively pushing the inner boundary of the outer radiation belt outward. This effect has been seen in images of the plasmasphere (seen via emission from He^+ ions) and ring current (seen via emissions from energetic neutral atoms), where the energetic ions in the ring current lie mainly outside of the plasmapause (Goldstein, 2006). Similar to the way the magnetosphere shields near-Earth space from the solar wind, the plasmasphere, when sufficiently dense, can shield space assets from the radiation belts.

1.2. Ring Current Contributions to Space Weather

The ring current has many space weather effects beyond magnetic perturbations at Earth's surface that are reported via the Dst index. It provides the seed population for the radiation belt electrons, which can be further energized by wave-particle interactions. It also carries the majority of the pressure in the inner magnetosphere and is therefore critical to the force balance in this region. Because this force balance distorts the geomagnetic field, magnetohydrodynamic models of the magnetosphere that include a model ring current tend to more accurately predict the magnetic field than magnetohydrodynamic models without the ring current (Glocer et al., 2013). Because the ring current is a significant source of particle precipitation into the upper atmosphere, it directly increases polar ionospheric electron densities and density gradients.

1.3. Uncertainty in the H Density

Recent calculations and recent measurements suggest that n_H values in the thermosphere, exosphere, and geocorona may be larger, or smaller, than previously computed. They are strongly suggestive that the functional form of $n_H(z)$ deviates from commonly used models. Two sources of uncertainty, or error, in $n_H(z)$ result directly from the physics. First, it is convenient to assume that the H population is thermalized. This approximation is used in the empirical MSIS (Emmert et al., 2014, MSIS is named for the mass spectrometer and incoherent scatter data upon which it was originally based) model thermosphere, where it may not always apply (see Qin & Waldrop, 2016, discussed below). In some cases, including the SAMI3 (Sami3 is Also a Model of the Ionosphere; Huba & Krall, 2013; Huba & Sazykin, 2014; Huba et al., 2017) ionosphere/plasmasphere simulations presented here, this approximation is used to extend MSIS density profiles into the exosphere. A second source of uncertainty comes from ion-neutral collisions in the exosphere, which remain physically significant at altitudes where the neutral species can be assumed to be collisionless. For example, in exosphere models that include separate ballistic, orbiting, and evaporative H populations, ion-neutral collisions couple these populations (Bishop, 1991). In the geocorona, the spherical approximation that neglects the neutral atom "geotail" is another source of error (Bailey & Gruntman, 2011; Carruthers et al., 1976; Østgaard et al., 2003; Rairden et al., 1986; Thomas & Bohlin, 1972; Zoennchen et al., 2011). According to Bishop (1991), this effect "is not very dramatic, amounting to a density enhancement of less than a factor of 2 in the antisolar direction for $r < 16\,R_E$." One aim of our study is to show that known uncertainties in n_H can significantly affect space weather.

Recent data analysis illustrates differences between measurements and current empirical models in the thermosphere and exosphere. For example, Qin and Waldrop (2016) analyzed Lyman-α measurements from the Global Ultraviolet Imager instrument (Paxton et al., 1999) on the Thermosphere Ionosphere Mesosphere Energetics and Dynamics (TIMED) spacecraft. They found evidence of incomplete thermalization of the upper thermosphere under all solar conditions. This condition was particularly pronounced for low solar activity, when the O density is significantly reduced, relative to solar maximum. An analysis of this same Global Ultraviolet Imager data from years 2002–2007, by Waldrop and Paxton (2013, Figures 14 and 15), showed deviations in $n_H(z)$ relative to MSIS. Here NRLMSISE-00 was used in the thermosphere, and the extension into the exosphere was based on the Bishop (1991) modification to the analytic approach of Chamberlain (1963). Deviations between empirical (MSIS exosphere) and data-driven, forward modeling results (the Bishop, 1991 exosphere with parameters adjusted to match observations) were often as large as a factor of 2.

Bishop et al. (2004) showed $n_H(z)$ profiles based on Fabry-Perot interferometer airglow measurements and satellite observations (at altitude ~ 570 km) of Lyman β obtained using the Espectrógrafo Ultravioleta extremo

para la Radiación Difusa instrument (García Primo, 2001). While their results do not uniquely determine the $n_H(z)$ profile, they certainly constrain $n_H(z)$. Factor of 2 differences between their data-based $n_H(z)$ profiles and MSIS-90 (Hedin, 1991) are not uncommon in both the exosphere and geocorona. Another comparison between MSIS and data is provided by Nossal et al. (2012). They compared H column emission intensities measured using the Wisconsin H-alpha Mapper Fabry-Perot to those calculated using NRLMSISE-00 with the Bishop (1991) exosphere extension. Measured intensities exceeded model intensities in all cases, with a ratio of 1.5 being typical. That the Nossal et al. (2012) results are sensitive to parameters affecting the exosphere extension model shows that these measurements capture density information from the thermosphere, exosphere, and geocorona.

Based on our current knowledge of $n_H(z)$ in the thermosphere and exosphere, and its uncertainty relative to current empirical models, we can suppose that $n_H(z)$ in the geocorona (the outermost part of the exosphere) is similarly uncertain. This uncertainty was illustrated by Ilie et al. (2013, Figure 1), where five geocorona H models are plotted for $2 < L < 6.5$, at local midnight, and for solar minimum conditions. Discrepancies were as large as a factor of 3. Ilie et al. (2013) begins with the simple, spherical, time-independent Rairden et al. (1986) model, which is also used in the ring current simulations of the present study. Also analyzed by Ilie et al. (2013) are models developed by Hodges (1994) who includes variations versus season and solar cycle based on Monte Carlo simulations, Nass et al. (2006), a modification of Hodges (1994) based on data from the Two Wide-angle Imaging Neutral-atom Spectrometers (TWINS) mission (McComas et al., 2009), and Bailey and Gruntman (2011), who expanded the Nass et al. (2006) model to add variation versus local time. However, recent work by Kameda et al. (2017) shows, using geocoronal images, that the H geocorona is not as elongated as in the Hodges (1994) or the related Zoennchen et al. (2013) models, suggesting that these models overstate the variation versus local time. While the ongoing model development suggests progress, the relationship between geocorona (e.g., altitude $> R_E$) H density and corresponding thermosphere and exosphere densities is not well known, especially on short (e.g., < 1 month) time scales. The degree of discrepancy between these models, noted above, does not necessarily suggest a similar degree of uncertainty in the H density. For example, the model with the largest H density, (Hodges, 1994), comes from a numerical analysis of the basic equations; it includes parameters, such as transport coefficients, that are not well established. When modified to better fit data (Ilie et al., 2013; Nass et al., 2006; Zoennchen et al., 2011), discrepancies between this and previous models are reduced.

In addition to varying versus solar cycle, season, and local time, the analysis of TWINS observations by Bailey and Gruntman (2013) shows that geomagnetic storms are associated with small (5–20%) spikes in geocoronal hydrogen density. Qin et al. (2017) find a similar affect using Thermosphere Ionosphere Mesosphere Energetics and Dynamics data: an upward redistribution of H density that reduces H in the topside ionosphere while increasing H in the geocorona during a storm. These increases, which last for hours and occur simultaneously with the downward spike in the Dst index, are so rapid that they may prove difficult to include in an empirical model.

A further source of uncertainty in $n_H(z)$, affecting the entire system, is our changing climate. In a climate-change sensitivity study by Nossal et al. (2016), a greenhouse gas doubling scenario was shown to produce increases in thermosphere H density of 40–50% (at altitude 400 km). In these simulations, each gas (CO_2, CH_4) produced an effect that varied differently with solar cycle producing a net increase of 50% at solar minimum and 40% at solar maximum. To be clear, a doubling of atmospheric CO_2 and CH_4 relative to a 1993 baseline, as considered in the sensitivity study of Nossal et al. (2016), is a significant increase that would have a profound effect on climate. Such levels do not reflect recent history but could occur within the current century (e.g. Pachauri & Meyer, 2014; Solomon et al., 2009).

1.4. Numerical Simulations

Simulations by Ilie et al. (2013), noted above, showed that varying the H density model can affect both the strength and morphology of the ring current. Past studies of the effect of the neutral atmosphere on plasmasphere refilling have been limited to the effect of the neutral oxygen, which forms a diffusive barrier (Lemaire & Gringauz, 1998), limiting refilling (Krall & Huba, 2016). The effect of the hydrogen exosphere on plasmasphere refilling remains largely unexplored.

In the following sections we present first-principle simulations using SAMI3 and the Comprehensive Inner Magnetosphere-Ionosphere (CIMI) model (Fok et al., 2014). This is followed by a discussion of space weather implications. We also discuss ongoing research efforts on this topic and the possibility of incorporating these

new results into operational space weather models. We conclude that improved and ongoing measurements of atmospheric composition in the thermosphere and exosphere are needed in addition to updated exosphere and geocorona models.

2. Models of Reduced and Enhanced H Scenarios

In the present study, we compute the impact of reduced H and enhanced H scenarios on plasmasphere refilling and on the ring current. By "reduced H" we mean an instance in which the H density is half that found in commonly used empirical models of the exosphere and geocorona. By enhanced H, we mean the H density is doubled relative to empirical models.

In this study we evaluate refilling following a model geomagnetic storm, using the Naval Research Laboratory SAMI3 ionosphere/plasmasphere model. SAMI3 (Huba & Krall, 2013; Huba & Sazykin, 2014; Huba et al., 2017) results compare favorably to measurements in the ionosphere (Shim et al., 2011) and plasmasphere (Krall et al., 2014).

For the plasmasphere simulations, H in the thermosphere and exosphere is specified using the most recent version of the empirical MSIS model, NRLMSISE-00 (Picone et al., 2002). For the thermosphere, the NRLMSISE-00 model is based on extensive data sets. Above the thermosphere, the NRLMSISE-00 model extends each species into the exosphere, based on a fixed scale height. Further out in the geocorona, NRLMSISE-00 H values deviate from a simple exponential, taking a form similar to a geocoronal model.

To simulate the ring current during a model geomagnetic storm, we use the CIMI model (Fok et al., 2014). CIMI self-consistently solves the bounce-averaged Boltzmann convection-diffusion equation for ring current particles O^+ and H^+. In CIMI, we specify H in the geocorona based on Rairden et al. (1986). CIMI is based on the earlier Comprehensive Ring Current Model, which compares well to geomagnetic index and imaging observations (Buzulukova et al., 2010).

We use a model thermosphere/exosphere based on MSIS, in SAMI3, and the Rairden et al. (1986) model geocorona, in CIMI. We do so to highlight current practice for these and similar plasmasphere and inner magnetosphere codes. One might argue that, prior to this study, we should update SAMI3 and CIMI to use more recent models or that we should use a common thermosphere/exosphere/geocorona model for both sets of simulations. However, the aim of this study is to highlight the fact that these models are in a state of flux and to explore the significance of the current state of uncertainty.

3. Impact of Hydrogen on Refilling

To show the impact of the reduced and enhanced hydrogen scenarios on poststorm plasmasphere refilling, we simulate a storm using the SAMI3 ionosphere/plasmasphere code (Huba & Krall, 2013; Huba et al., 2000). In each simulation we consider the refilling rate following a storm, during 3 days of refilling. We begin each run with two quiet days, to obtain a near steady state ionosphere/plasmasphere system. This is followed by an 8 h storm, beginning 0800 UT on the third day, and by three additional quiet days. Our model storm uses a simple Kp-driven Volland/Stern-Maynard/Chen (Maynard & Chen, 1975; Stern, 1975; Volland, 1973) polar cap electrostatic potential with Kp = 9 during the storm and Kp = 2 otherwise, where Kp is the planetary geomagnetic activity index.

Because refilling rates vary strongly with solar activity we consider both low and high solar activity. We set the $F_{10.7}$ extreme-ultraviolet index to either 80 (low activity) or 160 (high activity) and simulate the baseline, reduced H, and enhanced H scenarios at each setting. The $F_{10.7}$ index (Tapping, 2013) is a proxy for the old-fashioned "sunspot number" measurement.

An example is shown in Figure 1. Shown is the plasmasphere electron density in the magnetic equator (a) at storm onset, (b) during the storm, and (c) after 3 days of refilling. Also shown are electrostatic potential contours (white curves). These contours can be thought of as streamlines for $\mathbf{E} \times \mathbf{B}$ drifting "tubes" of magnetically trapped plasma (Siscoe, 1966). During the storm, most contours are open, so that plasma drifts out of the system, eroding the plasmasphere. After the storm, there are more closed contours near Earth and the plasmasphere refills. In this figure the Sun is off to the right. This shows the baseline case for low solar activity.

To measure refilling in each case, we compute the electron density in the magnetic equator, averaged over longitude. Results for the six cases are shown in Figure 2. Plotted is $\langle n_e \rangle$ at geocentric radii $4R_E$ (altitude 3 R_E)

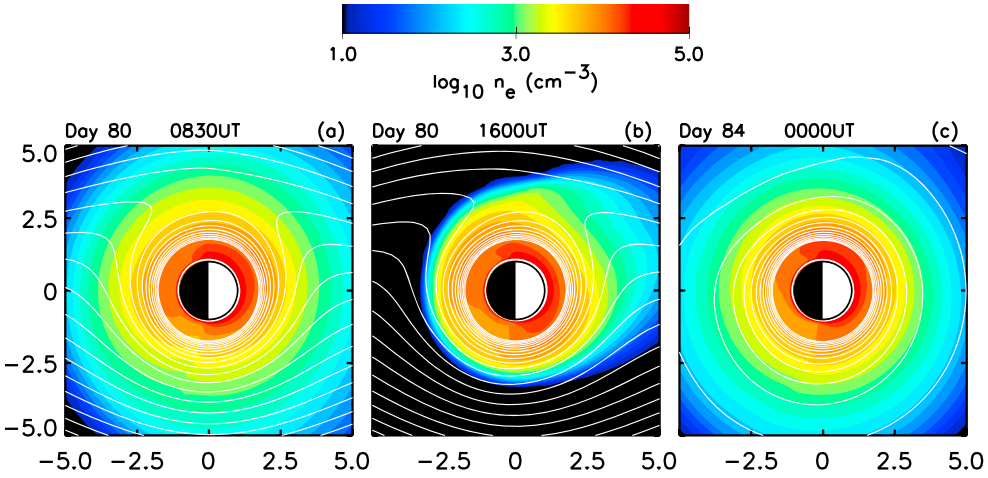

Figure 1. Color contours of n_e (log scale) in the equatorial plane from SAMI3 (a) at storm onset, (b) near the end of the model storm, and (c) at the end of the run. Contour lines indicate the potential.

and 5.2 R_E, corresponding to $L = 4.0$ and 5.2, where L is the McIlwain parameter (McIlwain, 1961). Poststorm refilling rates from these curves are shown in Table 1. In Table 1, we recover the well known but counter-intuitive result that refilling rates decrease with increasing solar activity (Rasmussen et al., 1993; Su et al., 2001). This finding became a paradox when it was shown that, when measured in terms of total electron content, the plasmasphere density appears to strengthen with increasing solar activity (Lee et al., 2013). The paradox was resolved by Krall and Huba (2016), who explored the sensitivity of the plasmasphere to the density of the oxygen exosphere.

Returning to the H exosphere, we find in all cases that reducing H by 0.5 reduces the refilling rate by a factor of 0.54–0.62; the effect is slightly stronger at high solar activity. Doubling the n_H nearly doubles the refilling rate in most cases. The increase ranges from a factor of 1.57 ($R/R_E = 5.2$, low activity) to 1.90 ($R/R_E = 4.0$, high activity). Again, the effect is stronger at high activity.

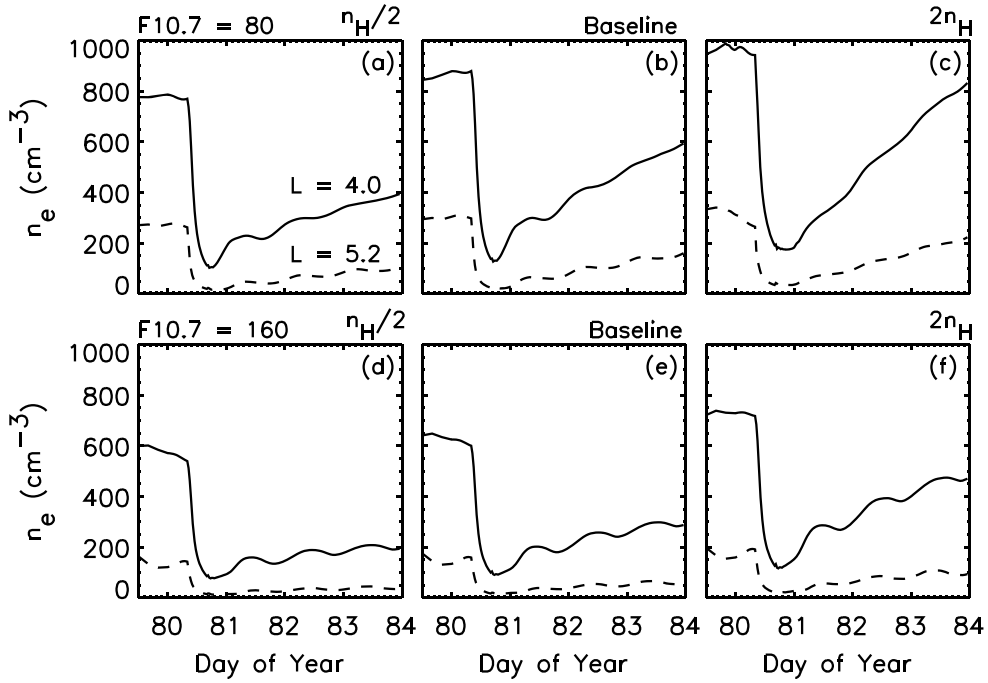

Figure 2. Electron density above the magnetic equator at geocentric radii $4R_E$ (solid) and $5.2R_E$ (dashed) for each case. The storm occurs on day 80.

Table 1
Refilling Rates (cm^{-3} d^{-1})

	Low activity			High activity		
R/R_E	Baseline	$n_H/2$	$2n_H$	Baseline	$n_H/2$	$2n_H$
4.0	120.	68.0	225.	51.6	27.9	97.8
5.2	40.0	24.6	62.6	12.9	7.48	23.6

We now illustrate the source of refilling in the upper thermosphere and lower exosphere. We plot profiles of atmospheric H and O and ionospheric H^+ and O^+ in Figure 3. Specifically, we show profiles along the $L=4$ magnetic field line, which, by definition, has its apex at $R/R_E=4.0$. Because the ionosphere/plasmasphere tends to breathe outward on the dayside and inward on the nightside (Galvan et al., 2008), a process that is apparent in the density plots of Figure 2, all profiles are averaged over the dayside. Shown are O, H, O^+, and H^+ versus height at the end of each simulation for the $n_H/2$ (a, d) and $2n_H$ (b, e) cases. Height profiles for the baseline case, not shown, would lie between these two cases. Of particular interest are ion profiles for the $n_H/2$ case (black) and the $2n_H$ case (red), compared in Figures 3c and 3f. Looking at Figure 3 we see that the ordering of the four cases, from high to low topside ionosphere H^+ density (at altitude 8,000 km), is $2n_H$/low (activity), $2n_H$/high, $n_H/2$/low, and $n_H/2$/high. This is the same as the ordering of the $L=4$ refilling rates in Table 1.

The correlation between the topside H^+ density and the refilling rate is consistent with Krall and Huba (2016, Figures 3 and 4) where it was the sensitivity of refilling to the thermosphere/exosphere O density, rather than the H density, that was under consideration. In all cases, refilling rates correlate strongly with the H^+ density above the O^+/H^+ transition height. Because the source of H^+ for refilling is the rapid $H+O^+ \rightleftharpoons H^+ + O$ charge exchange reaction (Geisler, 1967), refilling is affected by the transport of O^+ upward to the topside ionosphere (in SAMI3, each ion is a fluid that moves along the geomagnetic field against a background of ions and neutrals) and by the H density in the topside ionosphere.

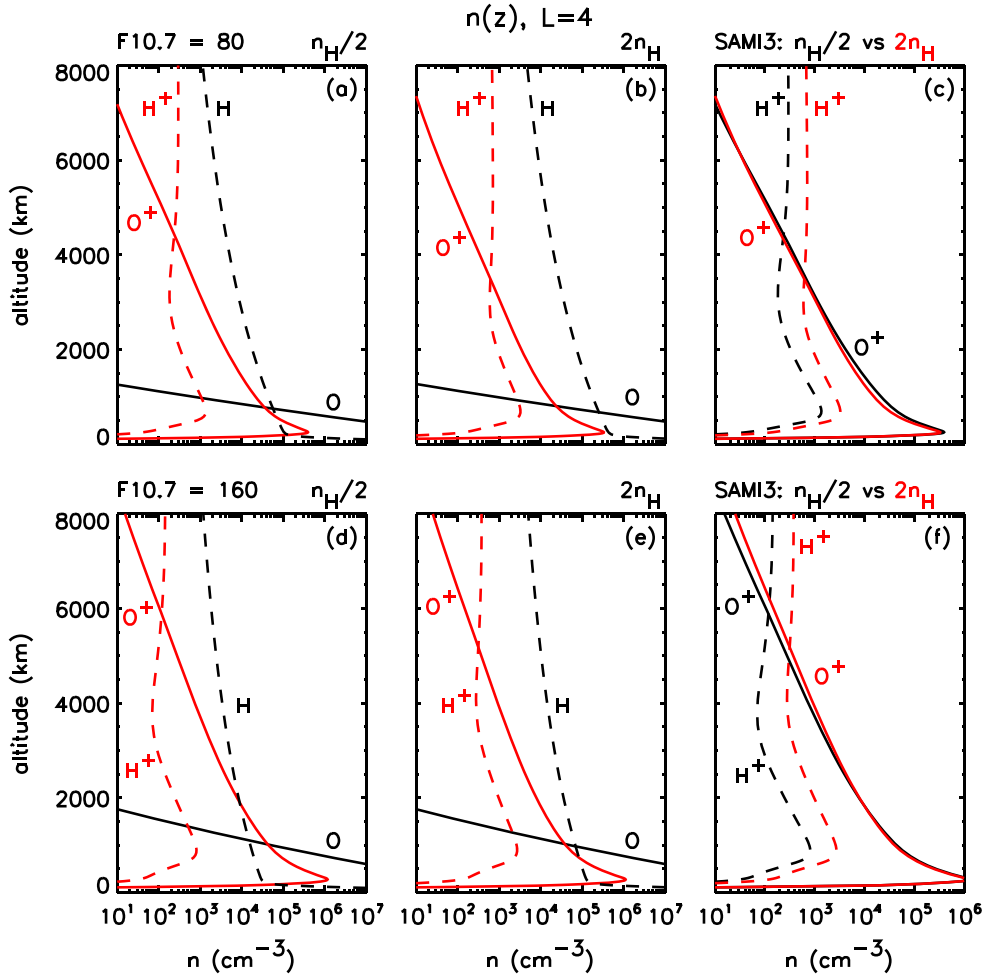

Figure 3. Average dayside profiles of O, O^+, H, and H^+ density are plotted versus position along a field line for $F_{10.7}=80$ (a–c) and 160 (d–f). Here we use a hydrogen-reduced (a, d) or hydrogen-doubled atmosphere (b, e). Ion profiles are compared in Figures 3c and 3f. SAMI = Sami3 is Also a Model of the Ionosphere.

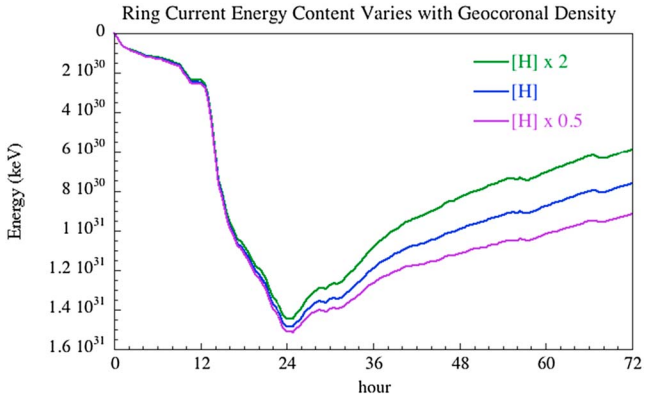

Figure 4. The ring current energy content during an average coronal mass ejection storm. The three different choices of geocorona density are shown. The typical value from Rairden et al. (1986) (blue), a case with the typical density multiplied by 2 (green), and the 0.5 case (purple).

4. Impact of Hydrogen on the Ring Current

The neutral exosphere density affects the ring current solution only through its contribution to charge exchange loss. In this process, energetic O^+ and H^+ ring current ions encounter cold exospheric neutrals, and the charge exchange reaction results in a cold ion and a hot neutral atom. This energetic neutral atom (ENA) can cross magnetic field lines to escape the ring current region. Charge exchange loss is particularly important during geomagnetic storms when the ring current is intense. This energy loss is one process leading to ring current decay and poststorm recovery. Indeed, it is speculated that when O^+ makes up a significant portion of the ring current, charge exchange loss becomes even more important as the O^+/H cross section, unlike the H^+/H cross section, remains large at high ion energies.

Emissions from ENAs, such as detected by TWINS or by the Imager for Magnetopause-to-Aurora Global Exploration spacecraft (Burch, 2000), are a direct measure of ring current energy lost to the geocorona. While ENA imaging is an excellent method for probing the ring current remotely, the density of the neutral exosphere is a major source of uncertainty (Ilie et al., 2013). In this section we examine the effect of exospheric uncertainty on ring current intensity during an average coronal mass ejection (CME) event.

To model the ring current, we use the CIMI model described in detail by Fok et al. (2014). CIMI solves the bounce-averaged Boltzmann equation for the distribution for ring current ions (0.1 keV to 400 keV) and electrons (1 keV to 4 MeV). Ions in CIMI originate from the plasmasheet boundary and are brought into the ring current by convection. In these simulations we use the plasma sheet boundary of Tsyganenko and Mukai (2003), which is driven by solar wind. The composition is specified using the Young et al. (1982) formulation, which is driven by Kp and $F_{10.7}$. Charge exchange with the neutral exosphere is represented as a loss term in the equation and appears as $-v\sigma_{sH}\langle n_H\rangle f_s$, where v is the ion velocity, σ_{sH} is the charge exchange cross section between ion species "s" and neutral hydrogen, $\langle n_H\rangle$ is the average density of neutral hydrogen along the field line, and f_s is the average distribution function for ion species s between the mirror points on a specified field line. The model includes a self-consistent calculation of the convection electric field and a realistic magnetic field. For full details of the model refer to Fok et al. (2014).

To look at ring current effects, we defined a typical CME storm based on a superposed epoch analysis of CME-type events using Van Allen Probe observations. We conducted a CIMI simulation with inputs selected to reproduce this typical storm, plus two additional simulations with the exospheric neutral H density either doubled or halved, relative to the baseline case. The default neutral exospheric hydrogen solution is taken from Rairden et al. (1986). We focus here on the total ring current energy content.

Figure 4 presents CIMI results for an average CME event with typical values of exospheric hydrogen from Rairden et al. (1986) (blue), a simulation with the typical density multiplied by 2 (green) and one with 0.5 (purple). The total ring current energy content is shown on the y axis, and the epoch time is shown on the x axis. The primary effect of geocoronal variation is to alter the poststorm recovery time scale. Generally speaking, the denser the geocorona the more rapidly the ring current decays. This result is consistent with the findings of Ilie et al. (2013): the density of the geocorona partially controls the charge-exchange loss, which is significant during and following the main phase of a geomagnetic storm.

5. Discussion

Above we present examples in which both the reduced and the enhanced H scenarios significantly affect model results. For either plasmasphere refilling or ring current dynamics, a factor of 2 in the H density has an effect large enough to spoil model data agreement found in the past (e.g., Buzulukova et al., 2010; Krall, Huba, et al., 2016) using previously assumed H density values. The point here is not that the models might be wrong. It is that our understanding of the inner magnetosphere will change if the H density turns out to be significantly different than assumed in the past. Specifically, plasmasphere refilling is sensitive to the H density in the topside ionosphere, while the ring current is sensitive to the H density in the geocorona.

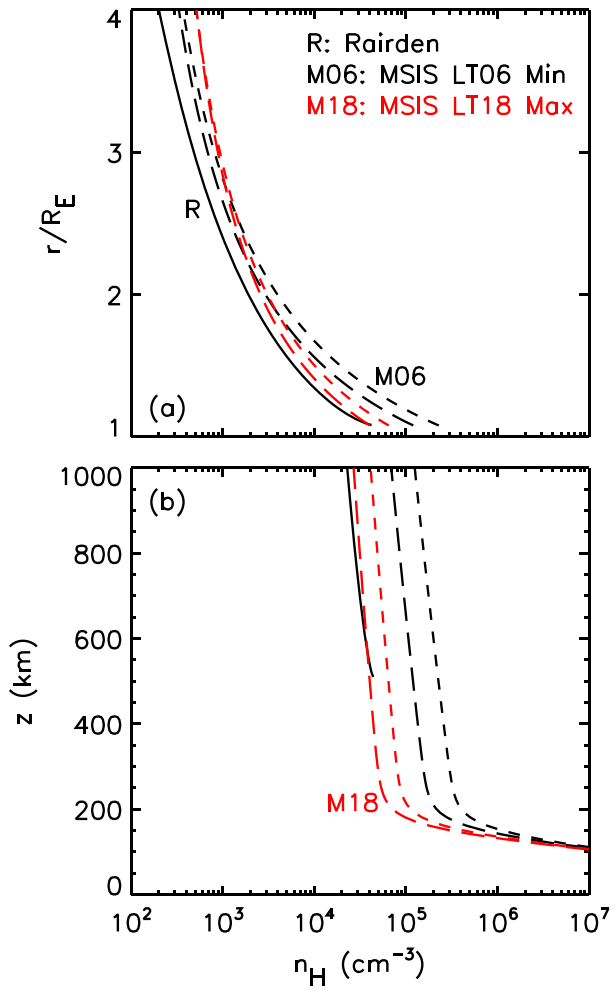

Figure 5. The Rairden et al. (1986) profile used in Comprehensive Inner Magnetosphere-Ionosphere (solid curves) is plotted in the (a) magnetosphere and (b) near Earth. The Mass Spectrometer Incoherent Scatter (MSIS) profile is similarly plotted at local times 0600 (short-dashed lines) and 1800 (long-dashed lines) and for solar minimum (black) and maximum (red) conditions.

In fact, even when a "state of the art" model agrees with the best available data, new measurements can introduce model data disagreement. This is hardly uncommon and always forces a useful reevaluation of each component of the model. Often the result is an improved understanding of the physical system as a whole. These simulations tell us that we cannot be confident in our understanding of the inner magnetosphere without accurate and ongoing measurements of the hydrogen density in the thermosphere, exosphere, and geocorona.

5.1. Simulation Results

From the simulations, it is clear that the H density in the exosphere affects the plasmasphere density. In particular, it affects the number of days (typically about 5) needed for the plasmasphere to recover to full saturated density after a storm. This result complements the work of Krall, Huba, et al., (2016); Krall, Emmert, et al. (2016), and Krall and Huba (2016), where the sensitivity of the plasmasphere to the O component of the exosphere was explored.

In Figure 4, we see that the H density significantly affects the rate at which energy is lost from the ring current, showing that higher H density leads to shorter storms and confirming the modeling result of Ilie et al. (2013). The Dessler-Parker-Sckopke formula (Dessler & Parker, 1959; Sckopke, 1966) relates the ring current energy density directly to the Dst index such that a more intense ring current means a more intense Dst. During the main phase of a storm, the ring current is replenished at a rate that dominates loss terms. As described by Daglis et al. (2003), ring current energy decay is initially dominated by the loss of energetic ions on "open" drift paths, followed by charge-exchange losses of ions on closed drift paths. Even as the ring current decays, both loss mechanisms remain significant.

For completeness, the profiles of the exosphere (MSIS) and geocorona (Rairden et al., 1986) H models used in this study are shown in Figure 5. The straight MSIS (dashed) curves above 500 km in Figure 5b demonstrate the fixed-scale height extension of the MSIS thermosphere into the exosphere. The curved profiles of Figure 5a show that, above 2,000 km, the NRLMSISE-00 model H density deviates from a simple exponential, as in the geocorona model (solid curve).

Figure 5 also illustrates the variation in the MSIS profile with local time and solar activity, as represented by $F_{10.7}$ values of 80 (representing solar minimum) and 160 (solar maximum). The MSIS profile also varies with season and geomagnetic activity but to a much lesser degree. The Rairden et al. (1986) profile used in CIMI does not vary. Because the plasmasphere is sensitive to near-Earth H densities while the ring current is sensitive to magnetospheric H densities, disagreements between each model and the actual conditions, as represented by observations, are perhaps more important than inconsistencies between the exosphere model and the geocorona model.

5.2. Next Steps

Clearly, an improved understanding of $n_H(z)$ is needed, including its dependence on latitude, local time, season, and solar cycle. Ongoing efforts to analyze large data sets should lead to significantly improved models within the next few years. In addition to ongoing studies, some of which are mentioned above (Gardner et al., 2017; Mierkiewicz et al., 2012; Nossal et al., 2012; Qin & Waldrop, 2016; Waldrop & Paxton, 2013), upcoming and proposed missions may shed light on this issue. For example, while not directly measuring composition, the Global-scale Observations of the Limb and Disk satellite (Eastes et al., 2013) will measure the exobase temperature an important parameter in thermosphere/exosphere models. Similarly, the proposed European SpaceCraft for the study of Atmospheric Particle Escape mission would measure the flux of major atmospheric components N and O escaping from Earth (Dandouras et al., 2017). Such measurements would significantly improve our understanding of exospheric physics and improve exosphere models.

Almost all present models assume that $n_H(z)$ is smoothly varying with latitude, local time, phase of the solar cycle, and season. Direct measurements of H density would test this assumption. A cubesat campaign, comprising Exocube and Exocube II, is designed to measure light-ion composition and transport in the exosphere. If successful, a mission of this type could be the first atmospheric mass spectrometer to measure atomic hydrogen (J. Noto, private communication, 2016).

Storm time interactions between the geocorona and the plasmasphere might also play a role. Recent TWINS observations (Zoennchen et al., 2017) show variation in n_H at high altitude (3–8 R_E) over the course of a geomagnetic storm. This suggests that an improved empirical n_H model may need to include dependences on geomagnetic indices such as Kp or Dst. Another example comes from the extreme ultraviolet spectrometer, EXtreme ultraviolet spectrosCope for ExosphEric Dynamics (EXCEED), on the Hisaki satellite. Here 20% variations in the column density of scattered geocoronal light generally tracked the *Dst* index, with maximum |Dst| corresponding to maximum geocoronal light (Kuwabara et al., 2017). In explaining this result, Kuwabara et al. (2017) suggest that charge exchange between the plasmasphere and the geocorona might play a role. We speculate that ion-neutral collisions between the refilling plasmasphere and the exosphere might also contribute to the excess neutral H observed in this circumstance.

Moving forward, it would be desirable to understand the day-to-day variability, if any, in the thermosphere, exosphere, and geocorona. Analysis of satellite drag shows that there is considerable variation, about 20%, in the globally averaged thermospheric density measured at altitude 400 km on a 4 day time scale (e.g. Krall, Emmert, et al., 2016, Figure 1). It is reasonable to suppose that n_H would have similar variations at this altitude. Unfortunately, global measurements of n_H on such short (4 day) time scales are beyond present capabilities.

6. Conclusions

These SAMI3 and CIMI simulations show that the H density in the exosphere and geocorona significantly affects space weather. The SAMI3 result, which is new, shows that the rate of plasmasphere refilling following a geomagnetic storm varies nearly linearly with the hydrogen density in the topside ionosphere. The CIMI result uses a state-of-the-art ring current model to confirm the finding of Ilie et al. (2013): storm time ring current decays more rapidly when H is increased in the geocorona.

Our modeling of reduced and enhanced hydrogen scenarios (relative to commonly used empirical H models) suggests that increased exosphere H density is associated with reduced threats to space assets during and following a geomagnetic storm. However, neither current n_H values nor the climate-driven rate of change in those values, if any, is well represented by current empirical models.

Based on the brief review of the literature (see section 1 above), the immediate need is for improved models of n_H in the thermosphere, exosphere, and geocorona that describe the variability of n_H with local time, season, and solar cycle. Current data analysis efforts (Gardner et al., 2017; Kuwabara et al., 2017; Mierkiewicz et al., 2012; Nossal et al., 2012; Qin & Waldrop, 2016; Waldrop & Paxton, 2013; Zoennchen et al., 2017) should provide n_H with enough resolution to support development of an improved model. However, we will need ongoing measurements so as to capture climate-driven changes in n_H.

Acknowledgments
This research was supported by NRL Base Funds and the NASA HSR Program, grant NNH14AX49I. A. G. and M. F. were supported by NASA Heliophysics Living With a Star Targeted Research and Technology program, under Work Breakdown Structure 936723.02.01.09.47. S. N. was supported by NSF, grant AGS-1343048. We thank Ed Mierkiewicz of Embry-Riddle Aeronautical University, John Noto of Scientific Solutions, Inc., Jianqi Qin of the University of Illinois at Urbana-Champaign, and Joel Fedder, formerly of Icarus Research, for helpful discussions. Numerical data associated with each of the figures are available from the publisher as supporting information for this publication.

References

Bailey, J., & Gruntman, M. (2011). Experimental study of exospheric hydrogen atom distributions by Lyman-alpha detectors on the TWINS mission. *Journal of Geophysical Research*, *116*, A09302. https://doi.org/10.1029/2011JA016531

Bailey, J., & Gruntman, M. (2013). Observations of exosphere variations during geomagnetic storms. *Geophysical Research Letters*, *40*, 1907–1911. https://doi.org/10.1002/grl.50443

Banks, P., Nagy, A., & Axford, W. (1971). Dynamical behavior of thermal protons in the mid-latitude ionosphere and magnetosphere. *Planetary and Space Science*, *19*(9), 1053–1067. https://doi.org/10.1016/0032-0633(71) 90104-8

Bishop, J. (1991). Analytic exosphere models for geocoronal applications. *Planetary and Space Science*, *39*(6), 885–893. https://doi.org/10.1016/0032-0633(91)90093-P

Bishop, J., Mierkiewicz, E. J., Roesler, F. L., Gómez, J. F., & Morales, C. (2004). Data-model comparison search analysis of coincident PBO Balmer α, EURD Lyman β geocoronal measurements from March 2000. *Journal of Geophysical Research*, *109*, A05307. https://doi.org/10.1029/2003JA010165

Borovsky, J. E., Denton, M. H., Denton, R. E., Jordanova, V. K., & Krall, J. (2013). Estimating the effects of ionospheric plasma on solar wind/magnetosphere coupling via mass loading of dayside reconnection: Ion-plasma-sheet oxygen, plasmaspheric drainage plumes, and the plasma cloak. *Journal of Geophysical Research: Space Physics*, *118*, 5695–5719. https://doi.org/10.1002/jgra.50527

Bortnik, J., & Thorne, R. (2007). The dual role of ELF/VLF chorus waves in the acceleration and precipitation of radiation belt electrons. *Journal of Atmospheric and Solar-Terrestrial Physics*, *69*(3), 378–386. https://doi.org/10.1016/j.jastp.2006.05.030

Burch, J. L. (2000). IMAGE mission overview. *Space Science Reviews*, *91*, 1–14. https://doi.org/10.1023/A:1005245323115

Buzulukova, N., Fok, M.-C., Goldstein, J., Valek, P., McComas, D. J., & Brandt, P. C. (2010). Ring current dynamics in moderate and strong storms: Comparative analysis of TWINS and IMAGE/HENA data with the Comprehensive Ring Current Model. *Journal of Geophysical Research*, *115*, A12234. https://doi.org/10.1029/2010JA015292

Carpenter, D. L. (1966). Whistler studies of the plasmapause in the magnetosphere. 1. Temporal variations in the position of the knee and some evidence on plasma motions near the knee. *Journal of Geophysical Research*, *71*, 693–709. https://doi.org/10.1029/JZ071i003p00693

Carruthers, G. R., Page, T., & Meier, R. R. (1976). Apollo 16 Lyman alpha imagery of the hydrogen geocorona. *Journal of Geophysical Research*, *81*(10), 1664–1672. https://doi.org/10.1029/JA081i010p01664

Chamberlain, J. W. (1963). Planetary coronae and atmospheric evaporation. *Planetary and Space Science*, *11*(8), 901–960. https://doi.org/10.1016/0032-0633(63)90122-3

Daglis, I. A., Kozyra, J. U., Kamide, Y., Vassiliadis, D., Sharma, A. S., Liemohn, M. W., … Lu, G. (2003). Intense space storms: Critical issues and open disputes. *Journal of Geophysical Research*, *108*(A5), 1208. https://doi.org/10.1029/2002JA009722

Dandouras, I., Yamauchi, M., Rème, H., Del Keyser, J., Marghitu, O., Fazakerley, A., … Tian, F. (2017). European Spacecraft for the study of Atmospheric Particle Escape (ESCAPE): A mission proposed in response to the ESA M5-call. In *19th EGU General Assembly, EGU2017* (5456 pp.). Vienna, Austria.

Dessler, A. J., & Parker, E. N. (1959). Hydromagnetic theory of geomagnetic storms. *Journal of Geophysical Research*, *64*(12), 2239–2252. https://doi.org/10.1029/JZ064i012p02239

Eastes, R. W., Mcclintock, W. E., Codrescu, M. V., Aksnes, A., Anderson, D. N., Andersson, L., … Woods, T. N. (2013). *Global-Scale Observations of the Limb and Disk (GOLD): New observing capabilities for the ionosphere-thermosphere* (pp. 319–326). Washington, DC: American Geophysical Union. https://doi.org/10.1029/181GM29

Emmert, J. T., McDonald, S. E., Drob, D. P., Meier, R. R., Lean, J. L., & Picone, J. M. (2014). Attribution of interminima changes in the global thermosphere and ionosphere. *Journal of Geophysical Research: Space Physics*, *119*, 6657–6688. https://doi.org/10.1002/2013JA019484

Fok, M.-C., Buzulukova, N. Y., Chen, S.-H., Glocer, A., Nagai, T., Valek, P., & Perez, J. D. (2014). The Comprehensive Inner Magnetosphere-Ionosphere model. *Journal of Geophysical Research: Space Physics*, *119*, 7522–7540. https://doi.org/10.1002/2014JA020239

Galvan, D. A., Moldwin, M. B., & Sandel, B. R. (2008). Diurnal variations in plasmaspheric He^+ inferred from extreme ultraviolet images. *Journal of Geophysical Research*, *113*, A09216. https://doi.org/10.1029/2007JA013013

García Primo, M. A. (2001). Spanish MINISAT program. Objectives and operational results. *Astrophysics and Space Science*, *276*(1), 3–12. https://doi.org/10.1023/A:1011669003999

Gardner, D. D., Mierkiewicz, E. J., Roesler, F. L., Harlander, J. M., Jaehnig, K. P., Nossal, S. M., & Haffner, L. M. (2017). First performance results of a new field-widened spatial heterodyne spectrometer for geocoronal Hα research. *Journal of Geophysical Research: Space Physics*, *122*, 1373–1385. https://doi.org/10.1002/2016JA022625

Geisler, J. E. (1967). On the limiting daytime flux of ionization into the protonosphere. *Journal of Geophysical Research*, *72*(1), 81–85. https://doi.org/10.1029/JZ072i001p00081

Glocer, A., Fok, M., Meng, X., Toth, G., Buzulukova, N., Chen, S., & Lin, K. (2013). CRCM + BATS-R-US two-way coupling. *Journal of Geophysical Research: Space Physics*, *118*, 1635–1650. https://doi.org/10.1002/jgra.50221

Goldstein, J. (2006). Plasmasphere response: Tutorial and review of recent imaging results. *Space Science Reviews*, *124*(1), 203–216. https://doi.org/10.1007/s11214-006-9105-y

Goldstein, J., Sandel, B. R., Forrester, W. T., & Reiff, P. H. (2003). IMF-driven plasmasphere erosion of 10 July 2000. *Geophysical Research Letters*, *30*(3), 1146. https://doi.org/10.1029/2002GL016478

Hedin, A. E. (1991). Revised global model of thermosphere winds using satellite and ground-based observations. *Journal of Geophysical Research*, *96*(A5), 7657–7688. https://doi.org/10.1029/91JA00251

Hodges, R. R. (1994). Monte Carlo simulation of the terrestrial hydrogen exosphere. *Journal of Geophysical Research*, *99*(A12), 23,229–23,247. https://doi.org/10.1029/94JA02183

Huba, J. D., & Krall, J. (2013). Modeling the plasmasphere with SAMI3. *Geophysical Research Letters*, *40*, 6–10. https://doi.org/10.1029/2012GL054300

Huba, J. D., & Sazykin, S. (2014). Storm time ionosphere and plasmasphere structuring: SAMI3-RCM simulation of the 31 March 2001 geomagnetic storm. *Geophysical Research Letters*, *41*, 8208–8214. https://doi.org/10.1002/2014GL062110

Huba, J. D., Joyce, G., & Fedder, J. A. (2000). SAMI2 (Sami2 is another model of the ionosphere): A new low-latitude ionosphere model. *Journal of Geophysical Research*, *105*(A10), 23,035–23,053. https://doi.org/10.1029/2000JA000035

Huba, J. D., Sazykin, S., & Coster, A. (2017). SAMI3-RCM simulation of the 17 March 2015 geomagnetic storm. *Journal of Geophysical Research: Space Physics*, *122*, 1246–1257. https://doi.org/10.1002/2016JA023341

Ilie, R., Skoug, R., Funsten, H., Liemohn, M., Bailey, J., & Gruntman, M. (2013). The impact of geocoronal density on ring current development. *Journal of Atmospheric and Solar-Terrestrial Physics*, *99*, 92–103. https://doi.org/10.1016/j.jastp.2012.03.010

Kameda, S., Ikezawa, S., Sato, M., Kuwabara, M., Osada, N., Murakami, G., … Fujimoto, M. (2017). Ecliptic north-south symmetry of hydrogen geocorona. *Geophysical Research Letters*, *44*, 11,706–11,712. https://doi.org/10.1002/2017GL075915

Krall, J., & Huba, J. D. (2016). The plasmasphere electron content paradox. *Journal of Geophysical Research: Space Physics*, *121*, 8924–8935. https://doi.org/10.1002/2016JA023008

Krall, J., Emmert, J. T., Sassi, F., McDonald, S. E., & Huba, J. D. (2016). Day-to-day variability in the thermosphere and its impact on plasmasphere refilling. *Journal of Geophysical Research: Space Physics*, *121*, 6889–6900. https://doi.org/10.1002/2015JA022328

Krall, J., Huba, J. D., Denton, R. E., Crowley, G., & Wu, T.-W. (2014). The effect of the thermosphere on quiet time plasmasphere morphology. *Journal of Geophysical Research*, *119*, 5032–5048. https://doi.org/10.1002/2014JA019850

Krall, J., Huba, J. D., Jordanova, V. K., Denton, R. E., Carranza, T., & Moldwin, M. B. (2016). Measurement and modeling of the refilling plasmasphere during 2001. *Journal of Geophysical Research*, *121*, 2226–2248. https://doi.org/10.1002/2015JA022126

Kuwabara, M., Yoshioka, K., Murakami, G., Tsuchiya, F., Kimura, T., Yamazaki, A., & Yoshikawa, I. (2017). The geocoronal responses to the geomagnetic disturbances. *Journal of Geophysical Research: Space Physics*, *122*, 1269–1276. https://doi.org/10.1002/2016JA023247

Lee, H.-B., Jee, G., Kim, Y. H., & Shim, J. S. (2013). Characteristics of global plasmaspheric TEC in comparison with the ionosphere simultaneously observed by Jason-1 satellite. *Journal of Geophysical Research: Space Physics*, *118*, 935–946. https://doi.org/10.1002/jgra.50130

Lemaire, J., & Gringauz, K. I. (1998). *The Earth's plasmasphere*. New York, NY: Cambridge University Press.

Maynard, N. C., & Chen, A. J. (1975). Isolated cold plasma regions: Observations and their relation to possible production mechanisms. *Journal of Geophysical Research*, *80*(7), 1009–1013. https://doi.org/10.1029/JA080i007p01009

McComas, D. J., Allegrini, F., Baldonado, J., Blake, B., Brandt, P. C., Burch, J., … Zoennchen, J. (2009). The Two Wide-angle Imaging Neutral-atom Spectrometers (TWINS) NASA mission-of-opportunity. *Space Science Reviews*, *142*(1), 157–231. https://doi.org/10.1007/s11214-008-9467-4

McIlwain, C. E. (1961). Coordinates for mapping the distribution of magnetically trapped particles. *Journal of Geophysical Research*, *66*(11), 3681–3691. https://doi.org/10.1029/JZ066i011p03681

Mierkiewicz, E. J., Roesler, F. L., & Nossal, S. M. (2012). Observed seasonal variations in exospheric effective temperatures. *Journal of Geophysical Research*, *117*, A06313. https://doi.org/10.1029/2011JA017123

Millan, R., & Thorne, R. (2007). Review of radiation belt relativistic electron losses. *Journal of Atmospheric and Solar-Terrestrial Physics*, *69*(3), 362–377. https://doi.org/10.1016/j.jastp.2006.06.019

Nass, H. U., Zoennchen, J. H., Lay, G., & Fahr, H. J. (2006). The TWINS-LAD mission: Observations of terrestrial Lyman-α fluxes. *Astrophysics and Space Sciences Transactions*, *2*(1), 27–31. https://doi.org/10.5194/astra-2-27-2006

Nossal, S. M., Mierkiewicz, E. J., & Roesler, F. L. (2012). Observed and modeled solar cycle variation in geocoronal hydrogen using NRLMSISE-00 thermosphere conditions and the Bishop analytic exosphere model. *Journal of Geophysical Research*, *117*, A03311. https://doi.org/10.1029/2011JA017074

Nossal, S. M., Qian, L., Solomon, S. C., Burns, A. G., & Wang, W. (2016). Thermospheric hydrogen response to increases in greenhouse gases. *Journal of Geophysical Research: Space Physics*, *121*, 3545–3554. https://doi.org/10.1002/2015JA022008

Østgaard, N., Mende, S. B., Frey, H. U., Gladstone, G. R., & Lauche, H. (2003). Neutral hydrogen density profiles derived from geocoronal imaging. *Journal of Geophysical Research*, *108*(A7), 1300. https://doi.org/10.1029/2002JA009749

Pachauri, R., & Meyer, L. (Eds.) (2014). *IPCC, 2014: Climate Change 2014: Synthesis Report. Contribution of Working Groups I, II and III to the Fifth Assessment Report of the Intergovernmental Panel on Climate Change*. In R. Pachauri & L. Meyer (Eds.). Geneva, Switzerland: IPCC.

Paxton, L. J., Christensen, A. B., Humm, D. C., Ogorzalek, B. S., Pardoe, C. T., Morrison, D., … Meng, C.-I. (1999). Global Ultraviolet Imager (GUVI): Measuring composition and energy inputs for the NASA Thermosphere Ionosphere Mesosphere Energetics and Dynamics (TIMED) mission. *Proceedings of SPIE*, *3756*, 265–276. https://doi.org/10.1117/12.366380

Picone, J. M., Hedin, A., Drob, D., & Aikin, A. (2002). NRLMSISE-00 empirical model of the atmosphere: Statistical comparisons and scientific issues. *Journal of Geophysical Research*, *107*, 1468. https://doi.org/10.1029/2002JA009430

Qin, J., & Waldrop, L. (2016). Non-thermal hydrogen atoms in the terrestrial upper atmosphere. *Nature Communications*, *7*, 13,655–13,661. https://doi.org/10.1038/ncomms13655

Qin, J., Waldrop, L., & Makela, J. J. (2017). Redistribution of H atoms in the upper atmosphere during geomagnetic storms. *Journal of Geophysical Research: Space Physics*, *122*, 10,686–10,693. https://doi.org/10.1002/2017JA024489

Rairden, R. L., Frank, L. A., & Craven, J. D. (1986). Geocoronal imaging with Dynamics Explorer. *Journal of Geophysical Research*, *91*(A12), 13,613–13,630. https://doi.org/10.1029/JA091iA12p13613

Rasmussen, C. E., Guiter, S. M., & Thomas, S. G. (1993). Two-dimensional model of the plasmasphere: Refilling time constants. *Planetary and Space Science*, *41*, 35–43. https://doi.org/10.1016/0032-0633(93) 90015-T

Schrijver, C. J., Dobbins, R., Murtagh, W., & Petrinec, S. M. (2014). Assessing the impact of space weather on the electric power grid based on insurance claims for industrial electrical equipment. *Space Weather*, *12*, 487–498. https://doi.org/10.1002/2014SW001066

Sckopke, N. (1966). A general relation between the energy of trapped particles and the disturbance field near the Earth. *Journal of Geophysical Research*, *71*(13), 3125–3130. https://doi.org/10.1029/JZ071i013p03125

Shim, J. S., Kuznetsova, M., Rastätter, L., Hesse, M., Bilitza, D., Butala, M., … Rideout, B. (2011). CEDAR Electrodynamics Thermosphere Ionosphere (ETI) challenge for systematic assessment of ionosphere/thermosphere models: NmF2, hmF2, and vertical drift using ground-based observations. *Space Weather*, *9*, S12003. https://doi.org/10.1029/2011SW000727

Siscoe, G. (1966). A unified treatment of magnetospheric dynamics with applications to magnetic storms. *Planetary and Space Science*, *14*(10), 947–967. https://doi.org/10.1016/0032-0633(66)90132-2

Solomon, S., Plattner, G.-K., Knutti, R., & Friedlingstein, P. (2009). Irreversible climate change due to carbon dioxide emissions. *Proceedings of the National Academy of Sciences of the United States of America*, *106*(6), 1704–1709. https://doi.org/10.1073/pnas.0812721106

Stern, D. P. (1975). The motion of a proton in the equatorial magnetosphere. *Journal of Geophysical Research*, *80*(4), 595–599. https://doi.org/10.1029/JA080i004p00595

Su, Y.-J., Thomsen, M. F., Borovsky, J. E., & Lawrence, D. J. (2001). A comprehensive survey of plasmasphere refilling at geosynchronous orbit. *Journal of Geophysical Research*, *106*(A11), 25,615–25,629. https://doi.org/10.1029/2000JA000441

Tapping, K. F. (2013). The 10.7 cm solar radio flux ($F_{10.7}$). *Space Weather*, *11*, 394–406. https://doi.org/10.1002/swe.20064

Thomas, G. E., & Bohlin, R. C. (1972). Lyman-alpha measurements of neutral hydrogen in the outer geocorona and in interplanetary space. *Journal of Geophysical Research*, *77*(16), 2752–2761. https://doi.org/10.1029/JA077i016p02752

Tsyganenko, N. A., & Mukai, T. (2003). Tail plasma sheet models derived from Geotail particle data. *Journal of Geophysical Research*, *108*(A3), 1136. https://doi.org/10.1029/2002JA009707

Volland, H. (1973). A semiempirical model of large-scale magnetospheric electric fields. *Journal of Geophysical Research*, *78*(1), 171–180. https://doi.org/10.1029/JA078i001p00171

Waldrop, L., & Paxton, L. J. (2013). Lyman α airglow emission: Implications for atomic hydrogen geocorona variability with solar cycle. *Journal of Geophysical Research: Space Physics*, *118*, 5874–5890. https://doi.org/10.1002/jgra.50496

Young, D. T., Balsiger, H., & Geiss, J. (1982). Correlations of magnetospheric ion composition with geomagnetic and solar activity. *Journal of Geophysical Research*, *87*(A11), 9077–9096. https://doi.org/10.1029/JA087iA11p09077

Zoennchen, J. H., Bailey, J. J., Nass, U., Gruntman, M., Fahr, H. J., & Goldstein, J. (2011). The TWINS exospheric neutral H-density distribution under solar minimum conditions. *Annales Geophysicae*, *29*(12), 2211–2217. https://doi.org/10.5194/angeo-29-2211-2011

Zoennchen, J. H., Nass, U., & Fahr, H. J. (2013). Exospheric hydrogen density distributions for equinox and summer solstice observed with TWINS1/2 during solar minimum. *Annales Geophysicae*, *31*(3), 513–527. https://doi.org/10.5194/angeo-31-513-2013

Zoennchen, J. H., Nass, U., Fahr, H. J., & Goldstein, J. (2017). The response of the H geocorona between 3 and 8 R_E to geomagnetic disturbances studied using TWINS stereo Lyman-α data. *Annales Geophysicae*, *35*(1), 171–179. https://doi.org/10.5194/angeo-35-171-2017